Summary

In this chapter, phenomenon of chromotropism in aminopyridine based tetrachlorocuprates has been investigated. Isomeric aminopyridines namely 2-, 3- and 4-aminopyridine (*ampy*) based tetrachlorocuprate(II) solids *viz.* (2-H*ampy*)$_2$[CuCl$_4$] (**6**), (3-H*ampy*)$_2$[CuCl$_4$] (**7**) and (4-H*ampy*)$_2$[CuCl$_4$].H$_2$O (**8**) were synthesized under ambient condition using solvent evaporation method upon reacting copper(II) chloride with aminopyridine (*ampy*) in the presence of hydrochloric acid. The structural elucidation of the synthesized solids was carried out using fourier transform infrared spectroscopy, CHN analyses, single crystal X-ray diffraction and powder X-ray diffraction. The thermal stability of the solids was established using thermogravimetric analysis and spin only magnetic moment was calculated by means of magnetic susceptibility measurements. In addition, a detailed investigation of the intermolecular interactions and proportion of contacts has been evaluated using Hirshfeld surface analyses and associated 2-D finger print plots. Solids **6-8** exhibited chromotropism particularly solvatochromism and vapochromism. In addition, **8** showed reversible thermochromism in the solid state. Solids **6-8** belong to Type IV of hybrid solids.

IV.1 Introduction

Chromotropism is the reversible or irreversible change in color of a substance due to the physical and chemical properties of its ambient surrounding medium, such as temperature, pressure, light, solvent and ions [1]. The type of hybrid solids in which the above phenomena occur most frequently is undoubtedly the area of coordination complexes (Type IV). Among the different types of coordinate compounds of copper(II), anionic halocuprate(II) complexes containing protonated organic moieties as counter-ions represent a unique category of hybrid solids. Interestingly, most of these solids reported in literature exhibit thermochromism (refer Table IV.1). Thermochromism is a special type of chromotropism in which a solid undergoes a change in color upon heating [2]. This unique feature can be attributed to the ability of $\{CuCl_4\}^{2-}$ units to exist as either tetrahedral or square-planar motifs. In most of the cases, usually the green $\{CuCl_4\}^{2-}$ square planar phase undergoes transformation into pale green or yellow colored $\{CuCl_4\}^{2-}$ tetrahedral phase upon heating [3]. On the other hand, a very few tetrachlorocuprate(II) anion based solids can undergo a change in color upon applying pressure i.e. piezochromism [4,5] as shown in Figure IV.1. However, only two examples of photochromism [6] in tetrachlorocuprate(II) anion based solids has been reported so far [7,8]. To the best of our knowledge, other forms of chromotropism particularly vapochromism [9,10] or solvatochromism [11,12] have not been explored in tetrachlorocuprate(II) anion based solids. Therefore, based on the above considerations, in this chapter an attempt has been made to synthesize tetrachlorocuprates based on three isomeric aminopyridines (*ampy*) and to explore their ability to act as chromotropic probes. Under our experimental conditions, reaction of copper(II) chloride with 2-, 3- and 4-*ampy* in the presence of hydrochloric acid resulted in solids *viz.* (2-H*ampy*)$_2$[$CuCl_4$] (**6**), (3-H*ampy*)$_2$[$CuCl_4$] (**7**) and (4-H*ampy*)$_2$[$CuCl_4$].H_2O (**8**) under ambient conditions.

Hirshfeld surface analyses and 2-D finger print plots revealed significant intermolecular interactions that stabilize the crystal structures. It was found that **6-8** exhibited solvatochromism and vapochromism. In addition, **8** showed reversible thermochromism in the solid state. It is noteworthy that solvatochromism and vapochromism in $\{CuCl_4\}^{2-}$ based hybrid solids have been demonstrated for the first-time using solids **6-8**.

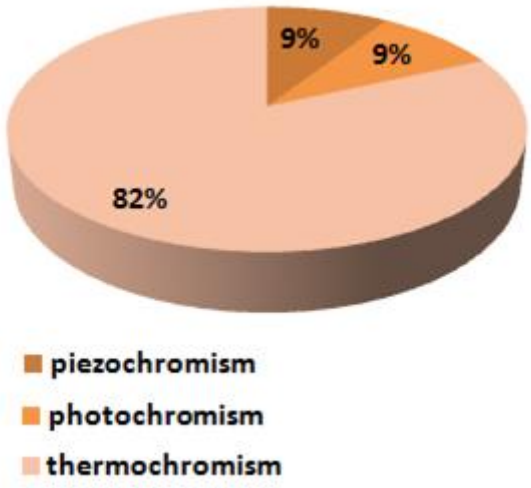

Figure IV.1 Figure showing the percentage of tetrachlorocuprate(II) anion based solids exhibiting thermo-, photo- and piezochromism.

Table IV.1 Literature review of Tetrachlorocuprate(II) solids exhibiting chromotropism.

S.No.	Solid	Cell parameters	Geometry of copper center	Synthesis	Chromotropic property	Ref.
1.	(DMe-DABCO)[$CuCl_4$] DMe-DABCO = N,N'-dimethyl-1,4-diazoniabicyclo[2.2.2] octane	Monoclinic, *Pca*2_1 *a* = 19.676Å, *b* = 8.083Å, *c* = 17.679Å β = 92°, Z = 8 Yellow crystals	Distorted tetrahedral geometry	Hydrothermal technique	Thermochromism	[3]
2.	(*pipz*H_2)[$CuCl_4$].$2H_2O$ (*pipz*H_2)$_2$[$CuCl_4$]Cl_2. $3H_2O$ *pipz*= piperazine	Monoclinic, *C*2/c *a* = 10.538Å, *b* = 7.431Å, *c* = 17.281Å β = 111.90°, Z = 4, Yellow crystals Triclinic, *P*-1 *a* = 9.264Å, *b* = 10.447Å, *c* = 11. 366 Å α = 68.38°, β = 82.86°, γ = 83.05°, Z = 2 Green crystals	Distorted tetrahedron Square planar geometry	Solvent evaporation	Thermochromism, Photochromism	[7]
3.	($C_4H_9NH_3$)$_2$[$CuCl_4$]	Cell parameters not reported. Golden sheet-like crystals	Distorted tetrahedron	Reflux followed by recrystallization	Photochromism	[8]
4.	[$CH_3C(NH_2)_2$]$_2$[$CuCl_4$] $CH_3C(NH_2)_2$ = acetamide	Monoclinic, *P*2_1/a *a* = 23.06Å, *b* = 7.93Å, *c* = 14.69Å β = 94.5°, Z = 4, Yellow plates	Distorted tetrahedral geometry	Solvent evaporation	Thermochromism	[13]

5.	$(C_2H_5NH_3)_2[CuCl_4]$	Orthorhombic, *Pbca* *a* = 21.18Å, *b* = 7.47Å, *c* = 7.35Å Z = 4, Yellow sheets	Square planar	Solvent evaporation	Thermochromism	[14]
6.	$[(NH_3CH_2CH_2)_2NH_2]Cl.[CuCl_4]$	Orthorhombic, *Pnma* *a* = 7.117Å, *b* = 23.78Å, *c* = 7.342 Å Z = 4 *a* = 7.15Å, *b* = 23.70Å, *c* = 7.36 Å Z = 4, Yellow, green, orange*	Square planar	Solvent evaporation	Thermochromism	[15]
7.	$[(CH_3)_2CHNH_3]_2[CuCl_4]$ $[(C_2H_5)_2NH_2]_2[CuCl_4]$	Triclinic, *P*-1 *a* = 7.245 Å, *b* = 14.588Å, *c* = 21.738Å *α* = 87.08°, *β* = 103.59°, *γ* = 104.73° Z = 6, Green needles**1a** Monoclinic, $P2_1/n$ *a* = 7.293Å, *b* = 14.881Å, *c* = 44.751Å *β* = 90.12°, Z = 12, Green needles**1b**	Distorted square planar geometry Distorted square planar geometry	Solvent evaporation Solvent evaporation	Thermo-Chromism**2**	**1a**. [16] **1b.** [17] **2.** [18]
8.	$[C_6H_5CH_2CH_2NHCH_3H]_2[CuCl_4]$	Monoclinic, $P2_1/c$ *a* = 6.495Å, *b* = 22.678Å, *c* = 8.584Å *β* = 116.08°, Z = 2, Green needles	Square planar geometry	Solvent exchange method	Thermochromism	[19]

9.	[*bzpipzn*] $[CuCl_4]0.5H_2O$ [*bzpipzn*][$CuCl_4$] *bzpipzn*= N-benzyl piperazine	Monoclinic, $P2_1/a$ *a* = 17.015Å, *b* = 16.977Å, *c* = 11.377Å β = 97.15°, Z = 8, Yellow crystals Monoclinic, $P2_1$ *a* = 12.075Å, *b* = 28.479Å, c = 9.925Å β = 109.54°, Z = 8, Green crystals	Moderately flattened tetrahedral geometry Unequally flattened tetrahedral	Solvent evaporation	Thermochromism	[20]
10.	Bis(dipropylammonium) tetrachlorocuprate(II)	Orthorhombic, *Pbca* *a* = 13.029Å, *b* =15.252Å, *c* = 20.997 Å Z = 8, Light green plates	Distorted tetrahedral geometry	Solvent evaporation	Thermochromism	[21]
11.	(*nmp*H)$_2$[$CuCl_4$] *nmp* = N-methylphenethyl amine) (N*phpip*H$_2$)[$CuCl_4$] N*phpip*=N-phenyl piperazine (N*bzpipz*H$_2$Cl)$_2$[$CuCl_4$] N*bzpipz* = N-benzyl piperazine (*tmba*)$_2$[$CuCl_4$] *tmba* = Trimethylbenzyl amine	Monoclinic, $P2_1/c$ *a* = 6.495Å, *b* = 22.678Å, *c* = 8.584Å β = 116.08°, Z = 2, Green needles[1a] Orthorhombic, $P2_12_12_1$ *a* = 17.698Å, *b* = 8.615Å, *c* = 9.841 Å Z = 4, Yellow-green crystals[1b] Monoclinic, *Pc* *a* = 21.954Å, *b* = 7.089Å, *c* = 9.139Å β = 97.054°, Z = 2, Green crystals[1c] Monoclinic, $P2_1/n$ *a* = 9.584Å, *b* = 9.104Å, *c* = 28.43Å β = 92.50°, Z = 4, Yellow leaflets[1d]	Square planar geometry Flattened tetrahedral geometry Extremely flattened tetrahedron Flattened tetrahedron	Solvent exchange method Solvent evaporation Solvent evaporation Solvent evaporation	Piezochromism[2]	**1a.** [19] **1b.** [22] **1c.** [23] **1d.** [24] **2**. [4]
12.	(p$CH_3C_6H_4NH_3$)$_2$	Orthorhombic, *Pbca*	Distorted	Solvent	Thermochromism[1a]	**1a**.[25]

	$[CuCl_4]$	a = 6.911Å, b = 7.052Å, c = 33.182 Å Flat sheet like yellow crystals[1a]	tetrahedral geometry	evaporation		**1b**.[26]
	$(pClC_6H_4NH_3)_2$ $[CuCl_4]$	Monoclinic, $P2_1/c$ a = 16.4359Å, b = 7.396Å, c = 7.262 Å β = 101.51°, Z = 2 Brown plate like crystals[1b]	Distorted tetrahedral geometry	Solvent evaporation		
13.	$(C_4H_6ClN_2S)_2[CuCl_4]$	Triclinic, P-1 a = 8.168Å, b = 10.919Å, c = 11.437 Å α = 64.24°, β = 80.03°, γ = 84.72° Z = 2, Amber colored crystals	Distorted tetrahedral geometry	Solvent evaporation	Thermochromism	[27]
	$(C_4H_7N_2S)_2[CuCl_4]$	Triclinic, P-1 a = 7.750Å, b = 8.474Å, c = 11.437 Å α = 64.24°, β = 80.03°, γ = 84.72°, Z = 2 Yellow colored crystals	Distorted tetrahedral geometry	Solvent evaporation		
14.	$(C_3N_3H_{10})_2[CuCl_4]$	Triclinic, P-1 a = 9.522Å, b = 11.215Å, c = 7.680 Å α = 93.85°, β = 100.41°, γ = 84.48°, Z = 2, Green-yellow crystals	Flattened tetrahedron	Solvent evaporation	Thermochromism	[28]
15.	$(C_5N_3H_8O)_2[CuCl_4]$	Triclinic, P-1 a = 11.053Å, b = 11.334Å, c = 14.038Å α = 95.76,β = 101.35, γ = 90.15°, Z = 4 Dark green crystals	Square planar geometry	Solvent evaporation	Thermochromism	[29]
16.	$(C_7H_{11}N_2)_2[CuCl_4]$	Monoclinic, $C2/c$ a = 11.973Å, b = 12.522Å, c = 14.523Å β = 113.86°, Z = 4 Parallelepiped shaped yellow crystals	Compressed tetrahedral geometry	Solvent evaporation	Thermochromism	[30]
17.	$2[(CNH_2)_3][CuCl_4]$.	Monoclinic, $P2_1/c$	Pseudo	Solvent	Thermochromism	[31]

	$2H_2O$	*a* = 8.084Å, *b* = 18.484Å, *c* = 16.939 Å *β* = 91.44°, Z = 8 Parallelepiped yellowish-green crystals	tetrahedral geometry	evaporation		
18.	$(C_7H_7N_2)_2[CuCl_4]$	Monoclinic, *C*2/*c* *a* = 14.903Å, *b* = 7.815Å, *c* = 16.130Å *β* = 92.93°, Z = 8, Yellow crystals	Distorted tetrahedral geometry	Solvent evaporation	Thermochromism	[32]
19.	$(C_8H_{12}N)_2CuCl_4$	Triclinic, *P*-1 *a* = 7.923Å, *b* = 9.150Å, c = 16.134Å *α* = 75.40°, *β* = 86.96°, *γ* = 64.49° Z = 2, Yellow crystals	Flattened tetrahedral geometry	Solvent evaporation	Thermochromism	[33]
20.	(EDBE)$[CuCl_4]$ EDBE= 2,2'-(ethylenedioxy)bis(ethyl ammonium)	Orthorhombic, *Pccn* *a* = 23.613Å, *b* = 7.594Å, *c* = 7.625Å Z = 4, Thin yellow - green plates[1]	Distorted tetrahedral geometry	Layering method	Thermochromism, Piezochromism[2]	**1.**[34] **2.**[5]
21.	[(R)-(+)-1-$C_{10}H_7CH(CH_3)NH_3$] $[CuCl_4]$	Monoclinic, $P2_1$ *a* = 12.715Å, *b* = 7.197Å, *c* =14.054Å *β* = 94.37°, Z = 2, Yellow crystals	Highly distorted tetrahedral geometry	Solvent evaporation	Thermochromism	[35]
	[(R)-(+)-2-$C_{10}H_7CH(CH_3)NH_3$] $[CuCl_4]$	Monoclinic, C_2 *a* = 10.796Å, *b* = 7.234Å, *c* =16.945Å *β* = 97.00°, Z = 2, Green crystals	Distorted square planar	Solvent evaporation	Thermochromism	
22.	$(C_7H_7N_2S)_2[CuCl_4]$	Monoclinic, $P2_1/c$ *a* = 6.952Å, *b* = 9.697Å, *c* = 13.963Å *β* = 97.84°, Z = 2, Green crystals	Square planar	Reflux followed by recrystallization	Thermochromism	[36]

* Yellow plates at room temperature (RT), pale green below RT, convert to orange brown on heating to 120°C

IV.2 Experimental

IV.2.1 Synthesis

Initially, (2-H*ampy*)$_2$[CuCl$_4$] (**6**), (3-H*ampy*)$_2$[CuCl$_4$] (**7**) and (4-H*ampy*)$_2$[CuCl$_4$].H$_2$O (**8**) were crystallized from a solution of CuCl$_2$.2H$_2$O, *ampy* and HCl in methanol or water as per the procedure given in literature by Kumar *et. al.*[37] and Halvorson *et. al.*[38] respectively. For the synthesis of **6** and **7**, Cu(II)acetate.2H$_2$O (198 mg, 1 mmol) was dissolved in water (10 mL) and concentrated HCl (4 mL). Subsequently, aminopyridine (188 mg, 2 mmol) in methanol (15 mL) was added and the solution was kept for crystallization at room temperature. On the other hand, crystals of **7** were obtained upon evaporation of a saturated solution of 4-*ampy* and CuCl$_2$.2H$_2$O in a dilute HCl solution. The cell parameter of the as-synthesized crystals was established by single crystal X-ray diffraction.

In the present work, however it was observed that **6**-**8** could be synthesized using only water as a solvent (Scheme IV.1). Initially, 10 mL of an aqueous solution of 2-*ampy* (0.553 g, 2 mmol) was added to an aqueous solution (10 mL) of CuCl$_2$.2H$_2$O (0.507 g, 1 mmol) and stirred using a magnetic stirrer. 5M HCl was added dropwise to obtain a clear blue solution having pH = 1.0±0.1. The resultant solution was left undisturbed for crystallization. After a few weeks, orange crystalline blocks of **6** were obtained (yield, 78.9% based on copper). The crystals were filtered, washed with water and acetone and dried in air. The same procedure was repeated using 3-*ampy* and 4-*ampy* and green crystalline blocks of solid **7** (yield, 77.5% based on copper) and yellow flakes of solid **8** (yield, 79.2% based on copper) respectively were obtained after a few weeks. The phase purity of the as-synthesized crystals was established by Rietveld analysis [39].

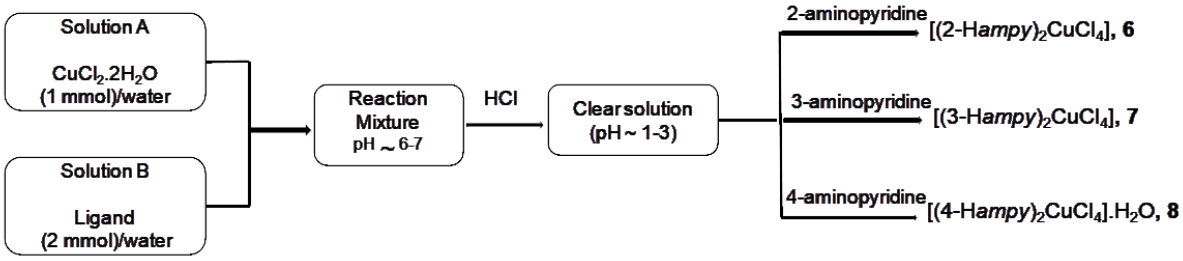

Scheme IV.1 Scheme showing the synthetic protocol.

IV.2.2 Characterization

The solids were characterized using techniques discussed under Section II.2.3 in Chapter II. Elemental analyses (C, H and N) were performed on ELEMENTAR Vario EL III CHNS Analyzer. The magnetic susceptibilities of the solids **6-8** were determined at room temperature using Guoy Balance (Sherwood, UK) and the spin only magnetic moment of the solids was calculated. The solid-state absorption spectra were recorded on a Jasco V-550 UV/Vis spectrophotometer in the range 200-800 nm. The electronic absorption spectra of **6-8** in different solvents were measured using Shimadzu UV-1800 spectrophotometer in the range 400-900 nm.

Results of CHN analysis of the bulk product were found to be consistent with the stoichiometry. Anal. Found:C, 30.01; H, 3.42; N, 14.08 %: Calcd: C, 30.30; H, 3.54; N, 14.15 % for **6**; Anal. Found: C, 30.25; H, 3.59; N, 14.50 %: Calcd: C, 30.30; H, 3.54; N, 14.15 % for **7** and Anal. Found: C, 21.06; H, 2.98; N, 10.42 %: Calcd: C, 21.53; H, 2.87; N, 10.05 % for **8**.

IV.2.3 Hirshfeld Surface Analyses

The molecular Hirshfeld surface analyses and their associated 2-D fingerprint plots (full and decomposed) were mapped employing the *CrystalExplorer* 21.5 program [40]. The CIF files of the solids were given as input [37,38]. The Hirshfeld surfaces were generated

using a standard (high) surface resolution. The 2-D fingerprint plots were displayed using the expanded 0.6–2.8Å range view with the d_e (distance from a point on the surface to the nearest nucleus outside the surface) and d_i (distance from a point on the surface to the nearest nucleus inside the surface) scales shown on the graph axes.

IV.2.4 Investigation of vapochromism

0.5 g of solid **6** was heated in a silica crucible at 100°C for 30 minutes and cooled in a desiccator for 2 hours. Thereafter, a small glass vial (10 mL capacity) containing 5 ml of double distilled water and the silica crucible were placed in a sealed glass jar for 18 hours. The same procedure was repeated with ammonia as another analyte. Similar experiments were performed with solids **7** and **8**.

IV.2.5 Investigation of solvatochromism

Solvatochromic property of the solids was investigated by measuring the absorption spectra of the solids in different solvents like water, ethanol, acetone and dimethyl formamide (DMF) in the range 400-900 nm. The concentration of the solutions was adjusted to 3×10^{-6} M.

IV.2.6 Investigation of thermochromism

0.5 g of solids **6-8** was heated at 120°C in a silica crucible for 15 minutes and then cooled to room temperature in order to establish the reversibility of the process.

IV.3 Results and Discussions

IV.3.1 Crystal structure description

The crystallographic details for solids **6-8** have been summarized in Table IV.2.

Table IV.2 Crystallographic details of solids **6-8**.

	6	**7**	**8**
Formula	$C_{10}H_{14}Cl_4CuN_4$	$C_{10}H_{14}Cl_4CuN_4$	$C_{10}H_{16}Cl_4CuN_4O$
Formula weight	395.59	395.59	557.45
T (K)	293(2)	293(2)	295(2)
Space Group	*P*-1	*P*-1	*C*2/*c*
a, Å	7.929(4)	7.9736(7)	8.457(2)
b, Å	8.115(3)	8.1332(8)	14.318(2)
c, Å	13.667(4)	13.6304(13)	14.382(2)
α, °	91.21(3)	91.231(2)	90
β, °	94.71(3)	94.731(2)	95.82(1)
γ, °	114.55(4)	115.009(10)	90
V, $Å^3$	795.71(50)	796.78(13)	1732.50(184)
Z	2	2	4
d_{calc}, $g \cdot cm^{-3}$	1.651	1.649	2.137
$\mu_{MoK\alpha}$, cm^{-1}	2.034	2.032	2.347
λ (Å)	0.70930	0.71073	0.71073
$R_1(I>2\sigma I)$, WR_2(all)	0.0576, 0.1572	0.0455, 0.1344	0.0349, 0.0750
GOF	1.109	1.089	1.055

The asymmetric unit in all the three solids showed $[CuCl_4]^{2-}$anionic moiety displaying a distorted tetrahedral geometry. Solids **6** and **7** crystallized in the space group *P*-1 in contrast to solid **8** which crystallized in a monoclinic crystal system with space group *C*2/*c* and it had an additional lattice water molecule. In all the three solids, only the pyridinium N atom was protonated, whereas the amine group was unprotonated, resulting in a charge of +1 for the organic cation. Solids **6** and **7** were found to be isostructural (Figure IV.2). In **6** and **7**, each $[CuCl_4]^{2-}$ unit was hydrogen bonded to surrounding protonated aminopyridine moieties to form 1-D chains (Figure IV.3) which were further

connected to form 3-D network (Figure IV.4). The crystal packing in **6** and **7** was also reinforced by π···π interactions between the protonated aminopyridine moieties. Also refer Table IV.3 and IV.4 for H-bonding interactions in **6** and **7**.

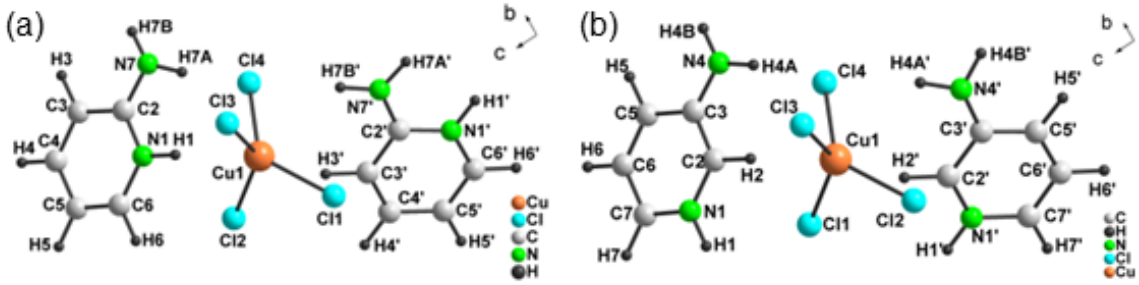

Figure IV.2 Asymmetric unit of (a) **6** and (b) **7**.

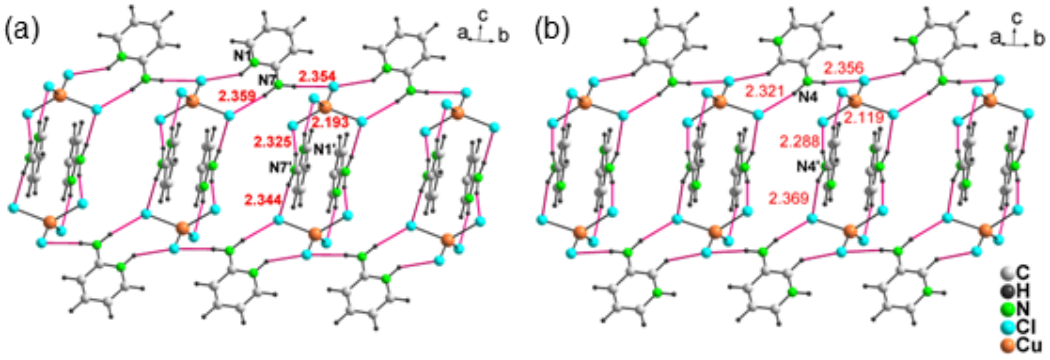

Figure IV.3 1-D chains formed via H-bonding interactions mediated by protonated aminopyridine moieties in (a) **6** and (b) **7**. Intra-chain H-bonding interactions are shown as red lines.

Table IV.3 H-bonding interactions in **6**.

D-H...A	D-H (Å)	H...A (Å)	D...A (Å)	∠ D-H...A (°)
N7-H7A···Cl	0.969(54)	2.359(69)	3.289(47)	160.71(3)
N1-H1···Cl2	1.009(14)	2.415(15)	3.230(35)	137.26(23)
N7-H7B···Cl4	0.995(47)	2.344(70)	3.334(80)	173.26(35)
N1-H1···Cl3	1.010(15)	2.193(14)	3.174(28)	163.40(24)
N7-H7B··· Cl2	0.982(42)	2.354(44)	3.333(7)	173.86(26)

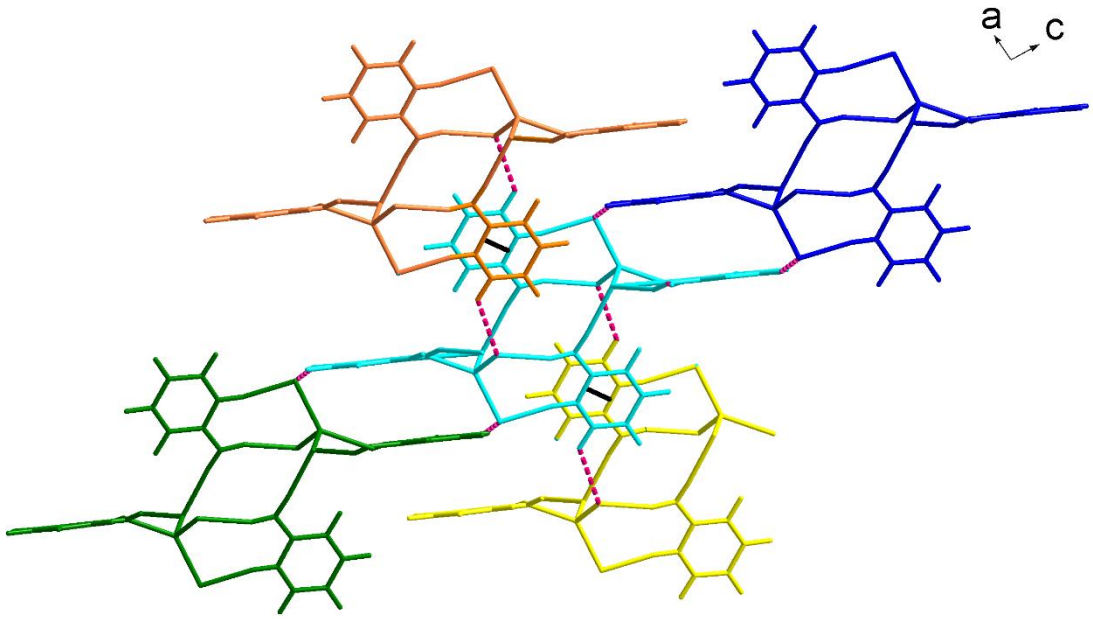

Figure IV.4 Through H-bonding interactions each 1-D chain is further extended into 3-D framework. Figure showing one chain (cyan) connected to four others (green, blue, orange, yellow). Inter-chain H-bonding interactions are shown in red dashed lines. Crystal packing in **6** and **7** is also facilitated by π···π interactions (3.767(31) and 3.779(1) Å respectively). π···π interactions are shown as black lines.

Table IV.4 H-bonding interactions in **7**.

D-H...A	**D-H (Å)**	**H...A (Å)**	**D...A (Å)**	**∠ D-H...A (°)**
N4-H4A···Cl4	0.983(59)	2.321(64)	3.289(5)	168.14(41)
N4-H4B···Cl1	0.995(39)	2.356(40)	3.344(5)	171.78(26)
N4-H4A···Cl4	0.992(38)	2.369(38)	3.330(6)	163.05(32)
N4-H4B···Cl2	0.989(34)	2.288(36)	3.260(5)	167.77(26)
C2-H2··· Cl4	1.081(3)	2.815(3)	3.726(4)	141.90(15)
C2- H2···Cl1	1.081(3)	2.367(1)	3.241(4)	136.86(16)
C5-H5···Cl3	1.081(3)	2.119(1)	3.167(4)	162.56(15)

Unlike, solids **6** and **7**, in **8** an additional lattice water molecule was observed in its asymmetric unit which enabled H-bonding interactions between $[CuCl_4]^{2-}$ units and water molecules to form 1-D chains propagating along *a* axis (Figure IV. 5). Through H-

bonding interactions each 1-D chain was further extended into 3-D framework (Figure IV. 6). Also refer Table IV.5 for H-bonding interactions in **8**.

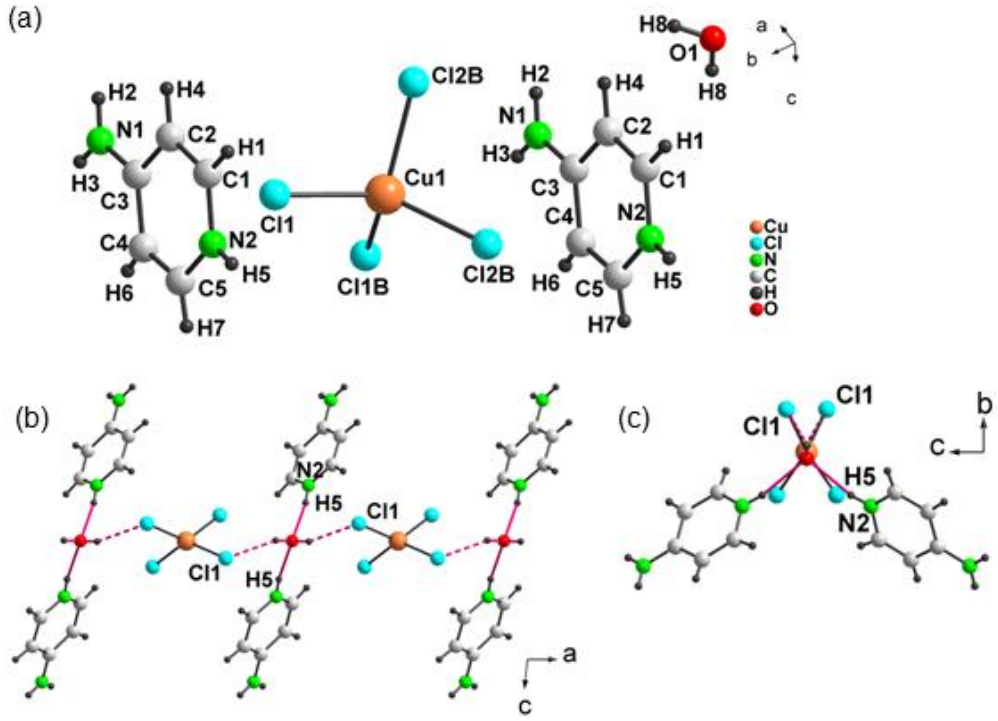

Figure IV.5 (a) Asymmetric unit in (4-H*ampy*)$_2$[CuCl$_4$].H$_2$O, **8**. (b) 1-D chains formed via H-bonding interactions mediated by protonated aminopyridine moieties and water molecule. H-bonding interactions mediated by lattice water molecule and $[CuCl_4]^{2-}$ are shown in red solid and dashed lines respectively. (c) View along *a* axis.

Table IV.5 H-bonding interactions in **8**.

D-H...A	**D-H (Å)**	**H...A (Å)**	**D...A (Å)**	∠ **D-H...A (°)**
N2-H5···O1	0.798(46)	2.040(46)	2.824(5)	166.99(446)
O1-H8···Cl1	0.800(29)	2.456(32)	3.224(6)	161.36(27)
N1-H3···Cl2	0.795(40)	2.585(40)	3.353(5)	162.96(37)
N1-H2···Cl1	0.803(44)	2.582(43)	3.367(11)	124.31(10)

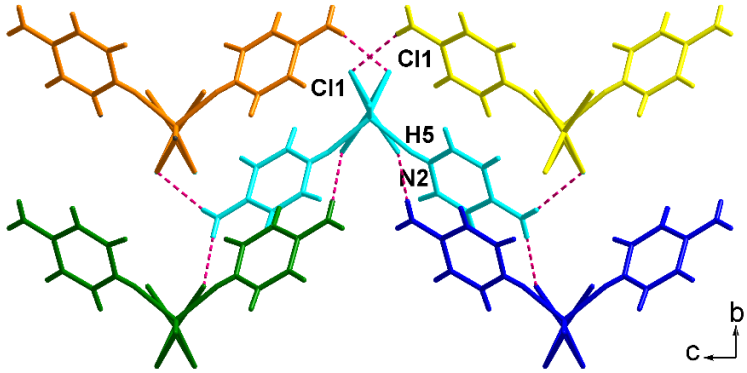

Figure IV.6 Through H-bonding interactions each 1-D chain is further extended into 3-D framework. Figure showing one chain (cyan) connected to four others (green, blue, orange, yellow). Inter-chain H-bonding interactions are shown in red dashed lines.

IV.3.2 Rietveld Analysis

Rietveld powder diffraction analysis of all the solids was carried out using GSAS to ensure homogeneity of the synthesized products. The phase purity of all the solids was established by Rietveld analysis and it was found that the cell parameters and space group from experimental powder data of bulk sample match well with those reported in literature [37,38]. Figures IV.7-9 represents Rietveld refinement of **6**-**8**. The red corresponds to the experimental data while black represents the calculated profile. The blue line gives the difference between the experimental and calculated diffraction profile.

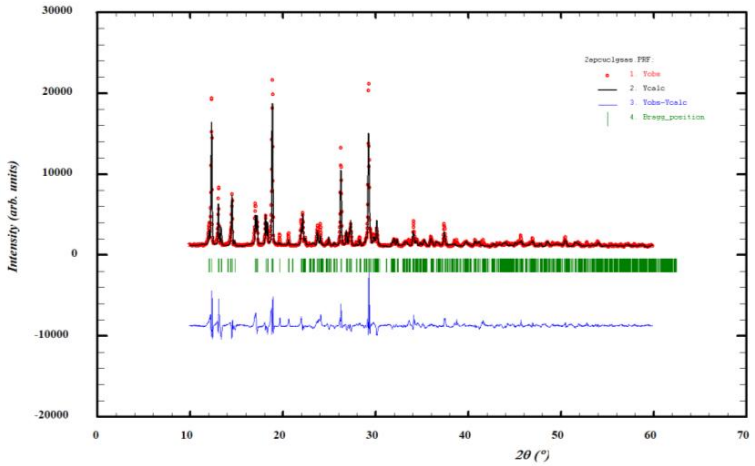

Figure IV.7 Rietveld refinement plot of **6.**

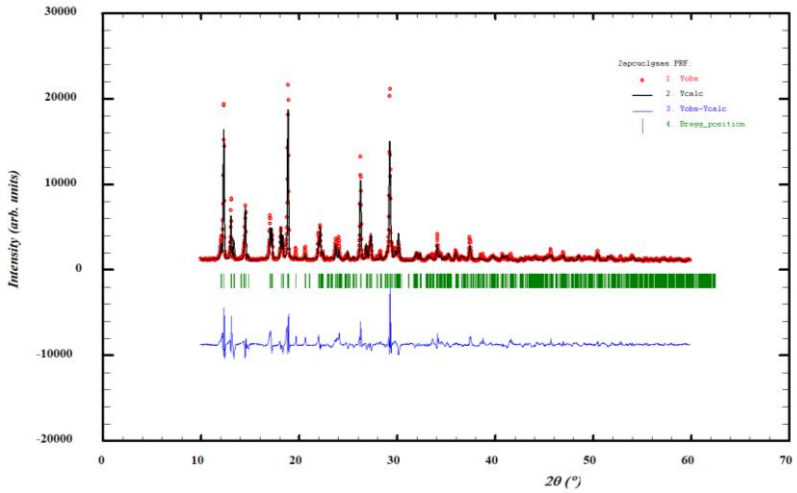

Figure IV.8 Rietveld refinement plot of **7.**

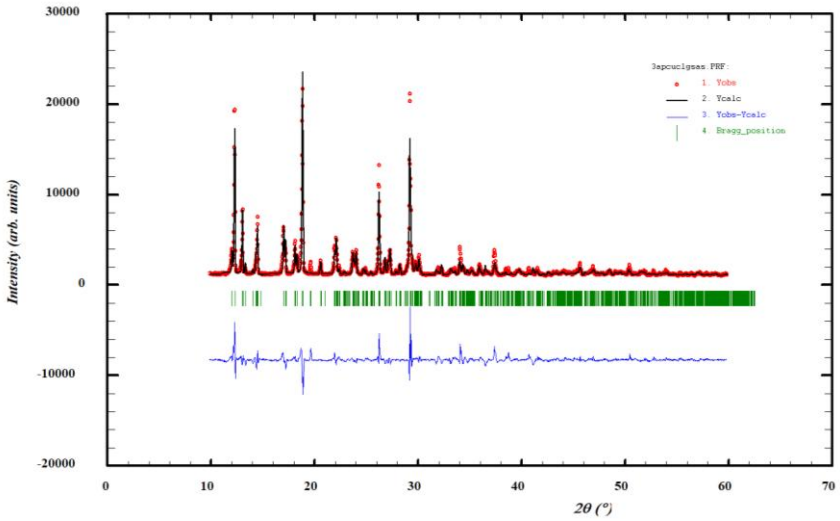

Figure IV.9 Rietveld refinement plot of **8.**

IV.3.3 Vibrational analyses

FTIR spectra of **6**-**8** showed a medium intensity band in the region 490-418 cm^{-1} due to Cu-Cl vibrations (Figure IV.10). The peaks due to N-H stretching vibrations could also be seen at around 3300-3100 cm^{-1}. The strong peaks in the range 1650-1540 cm^{-1} could be attributed to N-H bending vibrations [41]. A medium intensity band due to the C-N stretching was observed at around 1200 cm^{-1}.

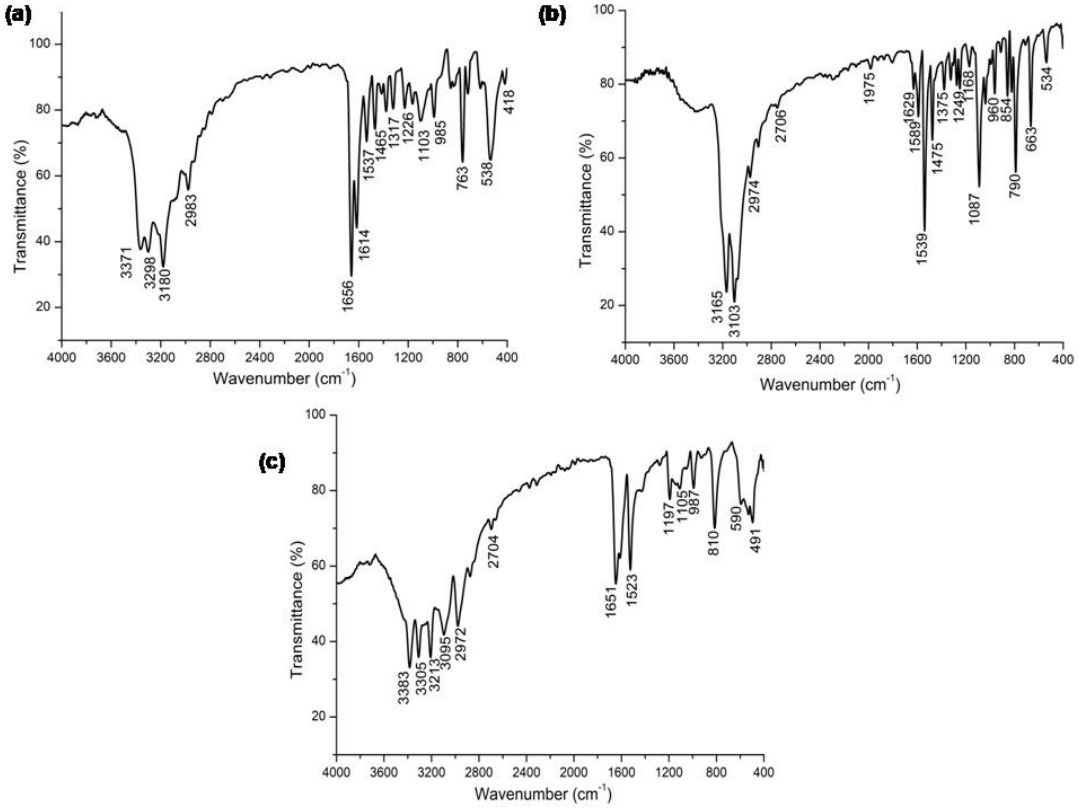

Figure IV.10 FTIR spectra of solids **6**-**8**.

IV.3.4 Thermal analyses

The thermal stability of solids **6**-**8** was established using TGA. For solids **6** and **7**, weight loss occurred in two consecutive steps in the temperature range of 160-330°C and 400-620°C, corresponding to the release of protonated aminopyridines and chloride ions respectively. The residual solid (~16%) could be attributed to elemental copper (Figure

IV.11). The TGA curve of **8** displayed three consecutive steps of weight loss in the temperature range 50-850°C which can be attributed to the loss of water molecule, aminopyridine moieties and chloride ions, leaving behind the residue of elemental copper (~19%) as shown in Figure IV.12. Differential Thermal Analysis (DTA) was also carried out to confirm the loss of lattice water molecule in **8**.

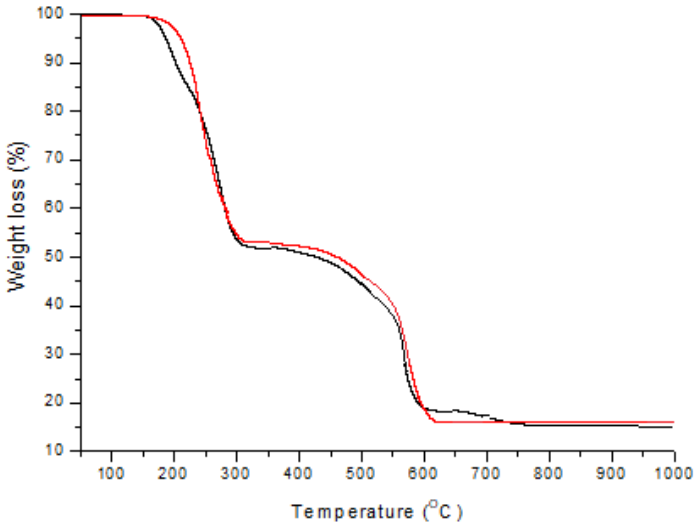

Figure IV.11 TGA curves of **6** and **7**.

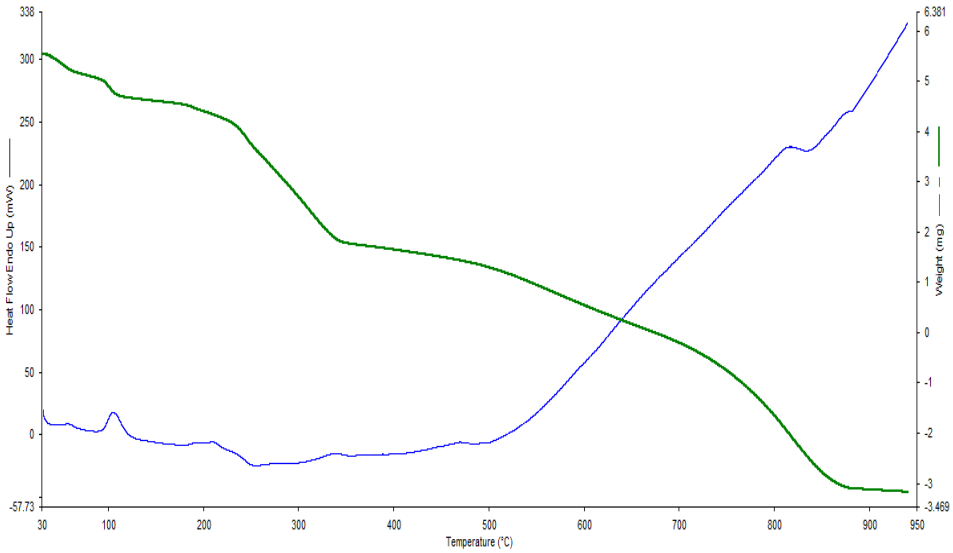

Figure IV.12 TGA-DTA curve of **8**.

IV.3.5 Magnetic studies

The spin only magnetic moment of the solids was found to be 1.4, 1.73 and 1.84BM for **6**, **7** and **8** respectively, which confirmed the +2 oxidation state of copper in **6-8**. The values were calculated using equations discussed under section III.2.3 in Chapter III. While **7** seemed to be paramagnetic in nature, a lower magnetic moment in **6** indicated anti-ferromagnetic interactions similar to those of related structures reported in literature [42, 43].

Table IV.6 Magnetic susceptibility measurements.

Solid	R_0	R	L (cm)	C	W (g)	χ_g	MW (g)	χ_m	μ (BM)
6	-24	100	1.8	1	0.1071	2.084×10^{-6}	395.5	0.861×10^{-3}	**1.4**
7	-29	118	1.7	1	0.0784	3.187×10^{-6}	395.5	1.26×10^{-3}	**1.73**
8	-29	86	1.6	1	0.0511	3.6×10^{-6}	413.5	1.422×10^{-3}	**1.84**

IV.3.6 Hirshfeld Surface Analyses

In order to get a deeper insight into various intermolecular interactions in the solids, the Hirshfeld surfaces (d_{norm}, d_i, d_e, shape index and curvedness) and 2-D fingerprint plots were generated using *Crystal Explorer 21.5* [40].

The Hirshfeld surfaces of **6** cover 374.05Å^2 area and spread over 388.96Å^3 volumes with 0.5 isovalue. The 3D d_{norm} surfaces were mapped over a fixed color scale of -0.468 to 1.308Å, the distance to the nearest nucleus inside the surface d_i ranging from 0.801 to 2.657Å, the distance to the nearest atoms outside d_e in the color scale of 0.800 to 2.554Å, whereas, shape index mapped within the color range of -1.000 to 1.000Å, and curvedness

in the range of -4.000 to 0.400Å respectively, as shown in Figure IV.13. The surfaces are shown transparent to permit visualization of the crystal structure. The bright red spots on the d_{norm} surface as shown in Figure IV.13a display short intermolecular contacts which mainly corresponds to N-H···Cl and C-H···Cl hydrogen bonding interactions. The appearance of consecutive red and blue triangular patches over the aromatic ring in the shape index map (Figure IV.13d) and large flat regions delineated by a blue outline on the curvedness map (Figure IV.13e) indicate the presence of weak π···π interactions in the crystal packing.

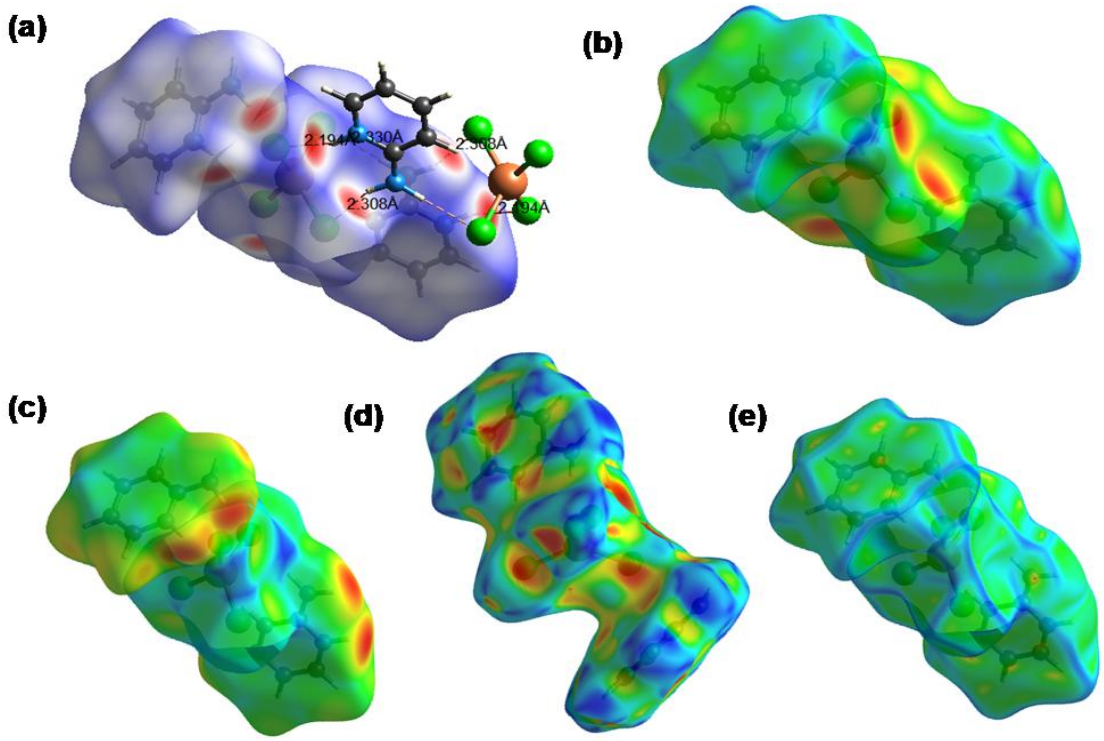

Figure IV.13 Hirshfeld surfaces for visualizing the intermolecular contacts in [(2-H*ampy*)$_2$CuCl$_4$], **6**. (a) d_{norm} highlighting the regions of N—H···Cl and C-H···Cl hydrogen bonds, (b) d_e, (c) d_i, (d) shape index and (e) curvedness.

The Hirshfeld surface of **7** spread over 360.14Å^2 area and holds 390.23Å^3 volume with 0.5 isovalue; the scaled color patches on the surface were generated in the range -0.523 to 1.348Å, 0.766 to 2.684Å, 0.766 to 2.545Å for d_{norm}, d_i and d_e respectively, whereas the shape index plot and curvedness plot are engendered from -1.00 to 1.00 a.u. and -4.000 to 0.400a.u., respectively, as shown in Figure V.14. Similar to **6**, red circular spots on the Hirshfeld surface of **7** indicate intermolecular close contacts of N-H···Cl and C-H···Cl hydrogen bonding interactions as shown in Figure V.14a. Shape index map and curvedness map shows the characteristic features of weak π···π stacking interactions in the crystal structure.

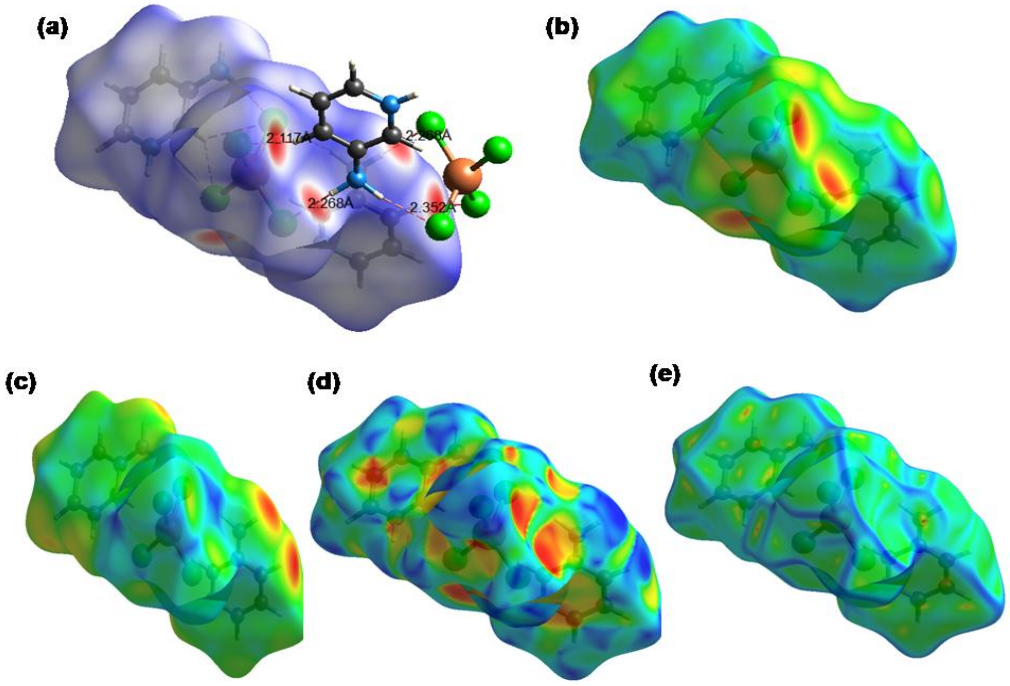

Figure IV.14 Hirshfeld surfaces for visualizing the intermolecular contacts in [(3-H*ampy*)$_2$CuCl$_4$], **7**: (a) d_{norm} highlighting the regions of N—H···Cl hydrogen bonds, (b) d_e, (c) d_i, (d) shape index and (e) curvedness.

The Hirshfeld surface of **8** cover 420.14Å^2 area and holds 490.23Å^3 volume with 0.5 isovalue; the scaled color patches on the surface were generated in the range -0.598 to 1.529Å, 0.745 to 3.195Å, 0.743 to 2.977Å for d_{norm}, d_i and d_e respectively, whereas the shape index plot and curvedness maps are plotted in the range -1.00 to 1.00 a.u. and -4.000 to 0.400a.u., respectively, as shown in Figure V.15. In **8**, the bright red circular spots on the surface correspond to N-H…Cl close contacts and also to H-bonding interactions mediated by water molecule. Shape index and curvedness plots suggests the presence of weak π···π stacking interactions similar to that in **6** and **7**.

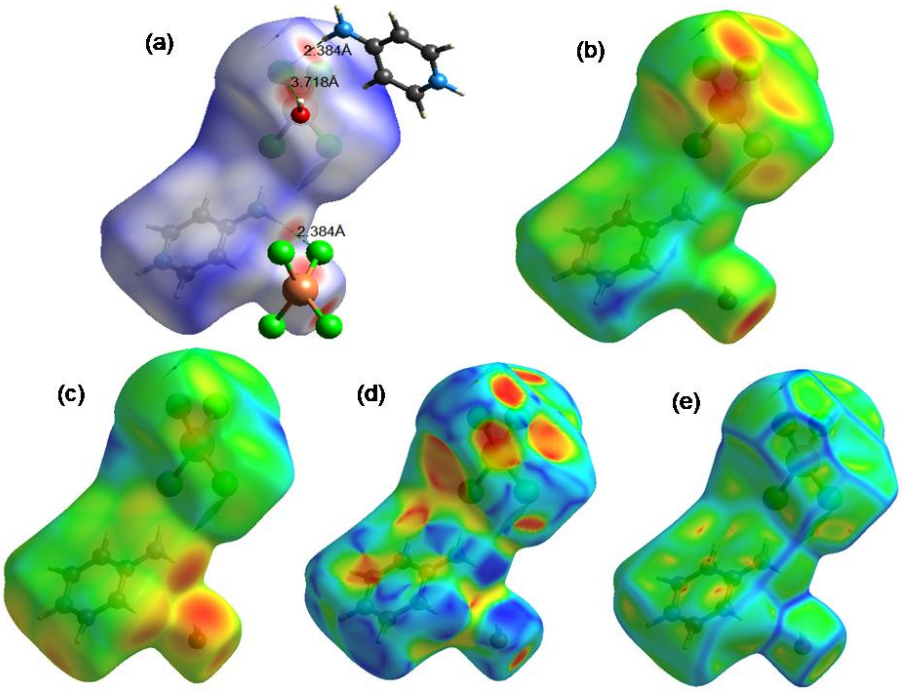

Figure IV.15 Hirshfeld surfaces for visualizing the intermolecular contacts in (4-H*ampy*)$_2$[CuCl$_4$].H$_2$O, **8**: (a) d_{norm} highlighting the regions of N-H···Cl and O-H···Cl hydrogen bonds, (b) d_e, (c) d_i, (d) shape index and (e) curvedness.

IV.3.6.1 Finger print plots

2-D finger print plots are an effective way for quantifying relative contribution of various intermolecular interactions that stabilize the crystal structure. The 2-D plot for overall and individual interactions in the crystal packing of **6**, **7** and **8** are shown in Figures IV.16-18 respectively**.** The most significant contact in all three solids was due to H···Cl/Cl···H contacts since it contributes 51.2% in **6**, 45.3% in **7** and 57.7% in **8** to the overall surface contacts. H···Cl/Cl···H contacts can be attributed to N-H···Cl and C-H···Cl hydrogen bonding interactions and appear as two sharp symmetric spikes in the finger print plots of **6-8** (refer Figures IV.16-18b).The second major contact is H···H, since it has a contribution of 25.9%, 27.2% and 19.8% in the crystal packing of **6**, **7** and **8** respectively. The C···H, N···H contacts also have significant contributions to the HS in all three solids as can be seen in the 2D plots. In **8**, another important contact is O···H contributing to 5.2% to the total surface due to the presence of water of crystallization.

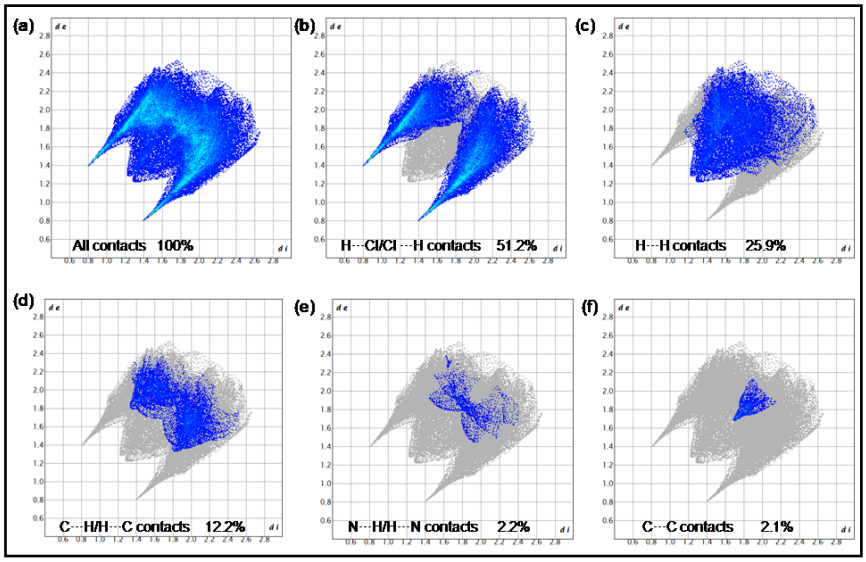

Figure IV.16 2-D fingerprint plots for **6** showing the contributions of different types of interactions: (a) all intermolecular contacts, (b) H···Cl/Cl···H contacts, (c) H···H contacts, (d) C···H/H···C contacts, (e) N···H/H···N contacts and (f) C···C contacts. The outline of the full fingerprint is shown in grey.

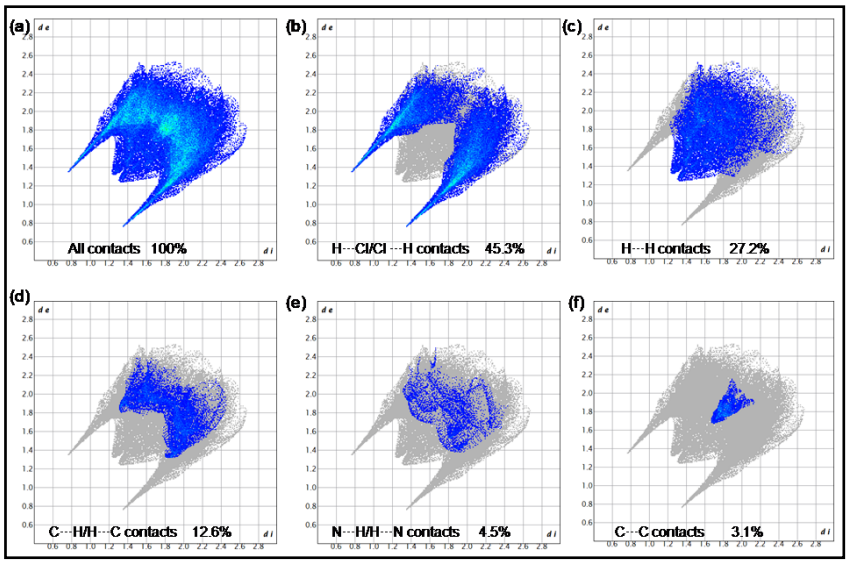

Figure IV.17 2-D fingerprint plots for **7** showing the contributions of different types of interactions: (a) all intermolecular contacts, (b) H···Cl contacts, (c) H···H contacts, (d) C···H/H···C contacts, (e) N···H/H···N contacts and (f) C···C contacts. The outline of the full fingerprint is shown in grey.

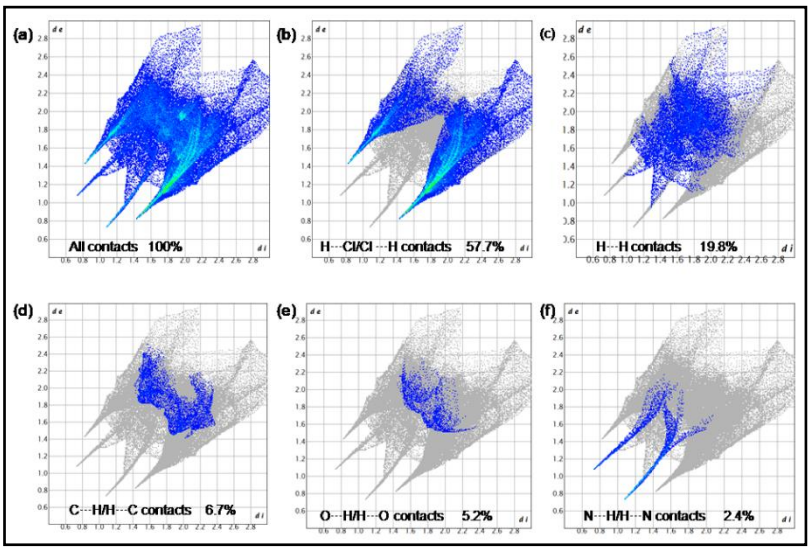

Figure IV.18 2-D fingerprint plots for **8** showing the contributions of different types of interactions: (a) all intermolecular contacts, (b) H···Cl contacts, (c) H···H contacts, (d) C···H/H···C contacts, (e) O···H/H···O contacts and (f) N···H/H···N contacts. The outline of the full fingerprint is shown in grey.

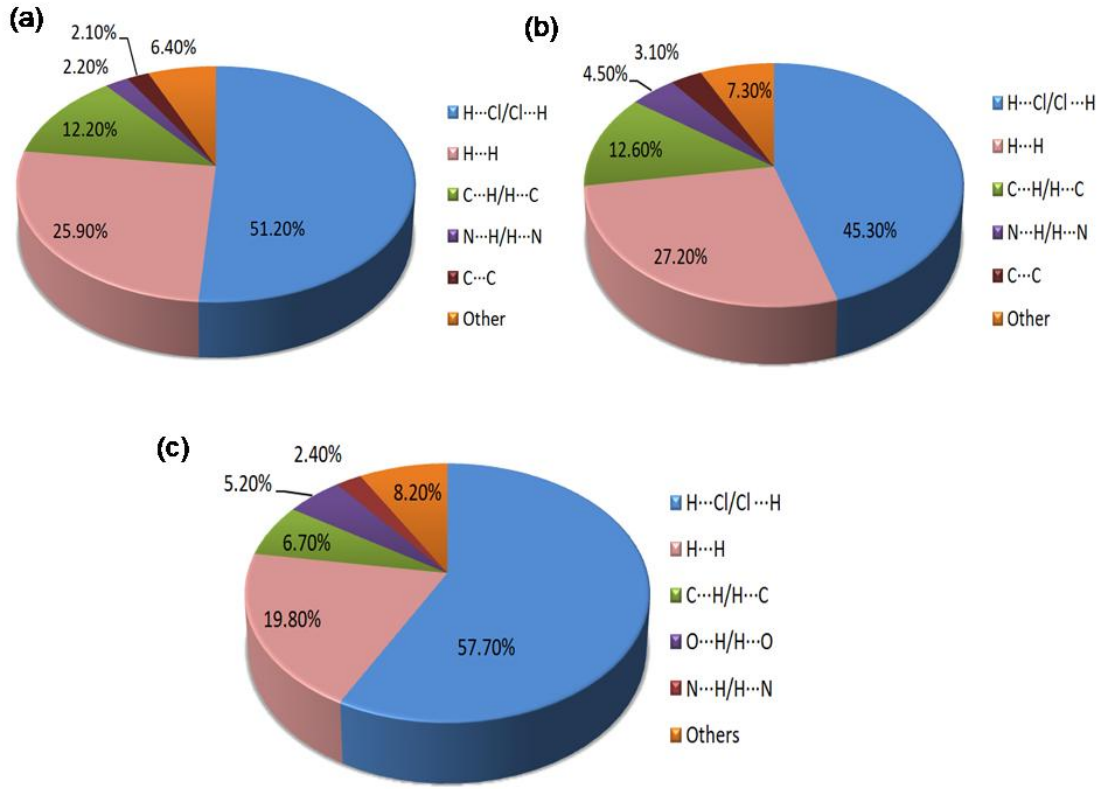

Figure IV.19 Graphical representation of the contribution of interatomic contacts in the crystal packing of (a) **6**, (b) **7** and (c) **8**.

IV.3.6.2 Crystal void analysis

The *Crystal Explorer 21.5* software can also be used to calculate the crystal voids contained in the solids, based on the electron density of the procrystal (0.002 au)-isosurface. Figure IV.20 gives a graphical representation of voids present in the crystal structure of solids **6**-**8**. The void volume in **6**, **7** and **8** corresponds to 75.85Å^3, 78.43Å^3 and 218.11Å^3 respectively; the surface area being 276.50Å^2, 283.48Å^2 and 671.94Å^2 respectively. The voids in solids appear to have occupied 9.53%, 9.84% and 12.58% of their respective unit cell volume. Thus, it can be inferred that cation and anion are strongly packed in the crystal structure.

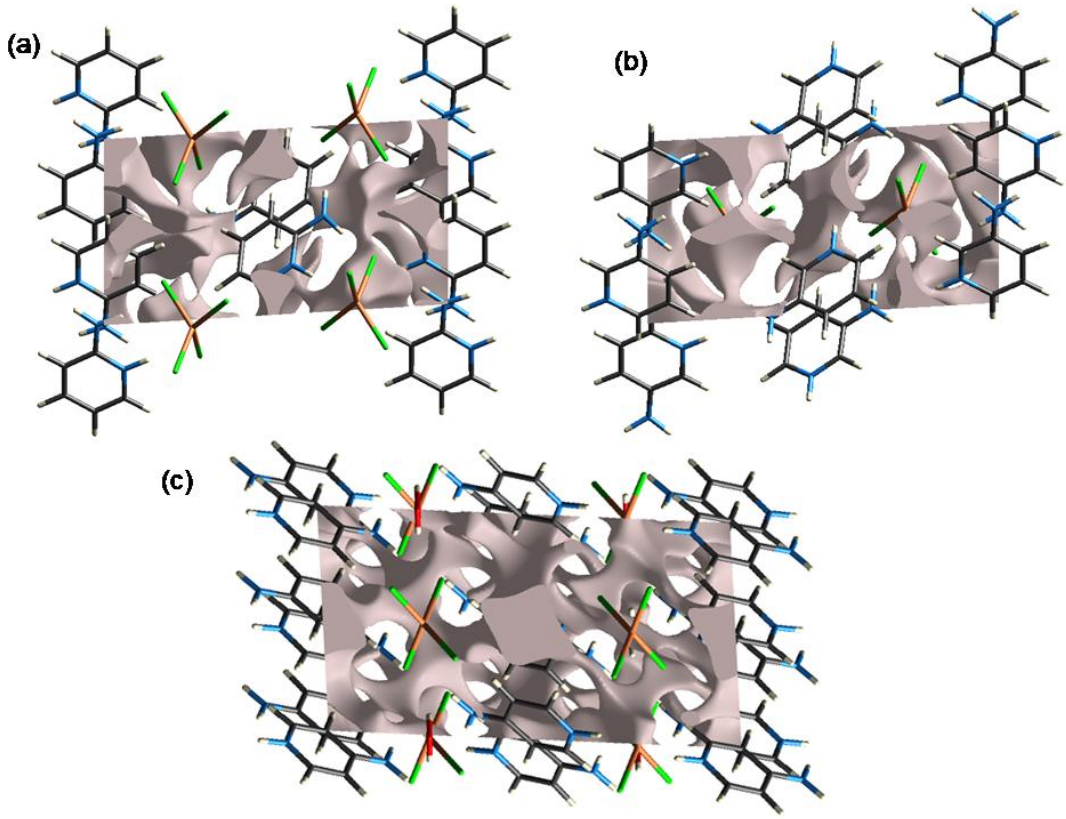

Figure IV.20 Graphical representation of void analysis along a crystallographic axis for solids (a) **6**, (b) **7** and (c) **8**.

IV.3.7 Chromotropism studies

The synthesized solids were found to exhibit chromotropic behavior particularly solvatochromism, vapochromism and thermochromism.

IV.3.7.1 Investigation of solvatochromism

The synthesized solids exhibited solvatochromism which was confirmed from the shift in absorbance peak in their electronic absorption spectra in different solvents as shown in Figure IV.21. From Figure IV.21, it was evident that **6-8** resulted in green colored solutions in polar protic solvents like water and ethanol and yellow colored solutions in polar aprotic solvents like DMF and acetone.

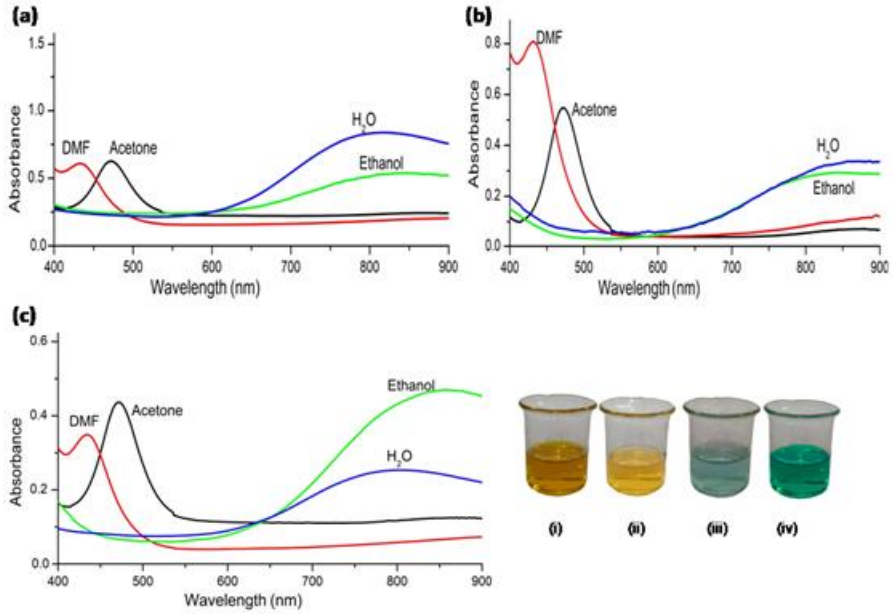

Figure IV.21 Absorption spectra of solids (a) **6**, (b) **7** and (c) **8** in different solvents. The image in the bottom right shows the color of the solids in solvents (i) DMF (ii) Acetone (iii) H_2O and (iv) Ethanol.

The UV-visible spectra of solids **6-8** exhibited similar patterns which are characteristic of $[CuCl_4]^{2-}$ species. Tetrachlorocuprates with tetrahedral symmetry exhibit ligand to metal charge transfer (LMCT) absorption bands in UV-visible region, usually ranging from 250-450 nm and weak d-d absorption bands are shifted into the near-IR region in the range 800-1400 nm [44]. LMCT absorption bands correspond to the symmetry allowed electronic transition from the ligand-localized molecular orbitals to the half-occupied d-orbital of the copper ion. The d-d absorption bands are due to symmetry forbidden electronic transition between the d-orbitals of the copper ion. In water and ethanol, a very broad d-d band was observed in the region near about 800-900 nm. The interaction of polar protic solvents with the solids results in solvation of Cu(II) ion and shows absorption maximum in the range 800-900 nm; being characteristic of copper(II) ion in a square planar structure. In DMF and acetone, bands were seen with maxima centered at

433 nm and 473 nm respectively which are the charge-transfer bands characteristic of $[CuCl_4]^{2-}$ species. Since $CuCl_4$ in DMF and acetone have no d-d transition bands below 900 nm, it can be inferred that solids retain their D_{2d} flattened tetrahedral structure in solutions of DMF and acetone. A similar observation has also been reported by Max Elleb *et.al*. [45]. Extensive hydrogen bonding interactions of solids with the solvent molecules also play a crucial role in shifting the absorption peaks.

IV.3.7.2 Investigation of vapochromism

All the solids were examined for their ability to act as vapochromic sensors and promising results were obtained. **6** and **8** and showed distinct visible color changes in presence of vapors of H_2O and NH_3 (Figure IV.22). The color change in **7** when exposed to the above vapors was not visible owing to its dark color. Vapochromic response was not observed with other volatile organic compounds like acetone, benzene, nitrobenzene, diethyl ether and phenol. **6** and **8** were found to be extremely sensitive to ammonia. They showed a change in color within 6 minutes of exposure to ammonia whereas a response time of 30 minutes was observed for water.

The solids when exposed to water showed green color and were hygroscopic. Further, the hydrated solids if left undisturbed under ambient environment for 3 days reverted back to the original state. However, the reversibility of color change occurred easily upon heating to 100°C for 12 minutes. On the other hand, **6** and **8** exposed to ammonia upon heating displayed interesting color variations. When heated at 100°C, the blue color changed to bright green. The green form when further exposed to ammonia changed to blue again which reversed to its green color upon heating. Therefore, the color change was found to be reversible. The green solid upon further heating turned black.

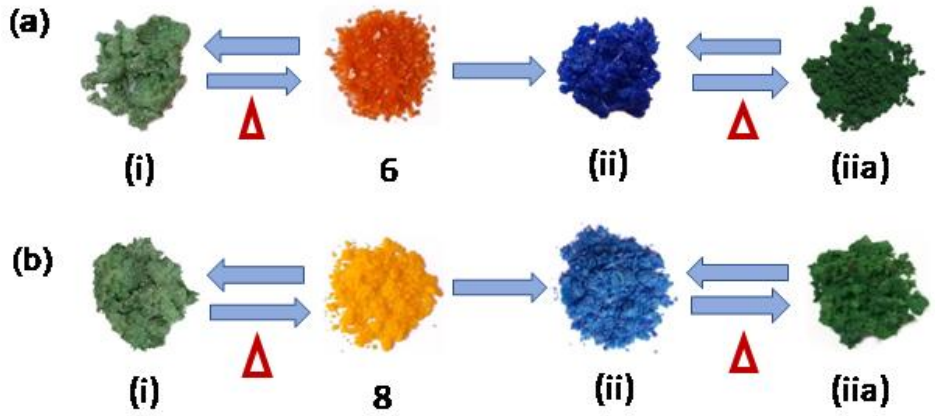

Figure IV.22 Vapochromic response of (a) **6** and (b) **8** to vapors of (i) H_2O and (ii) NH_3; (iia) shows the color change upon heating (ii).

Due to the hygroscopic nature of **6** exposed to ammonia, a detailed study of vapochromic phenomena was able to conduct only for **8** in the solid state using PXRD, UV-visible absorption spectroscopy and TGA. A comparison of PXRD pattern of the pure solid and solid **8** exposed to NH_3 vapors, showed a considerable shift in the peak positions (Figure IV.23). The alternate arrangement of tetrachlorocuprate anions and organic cations in the crystal packing apparently produces a porous structure as evident from the crystal void analysis (Figure IV.20). The void volume in solid **8** was calculated to be 218.11 $Å^3$ from the crystal void analysis. Incorporation of the vapors into the porous lattice plausibly perturbed the cation-anion stacking structure and caused changes in the PXRD patterns.

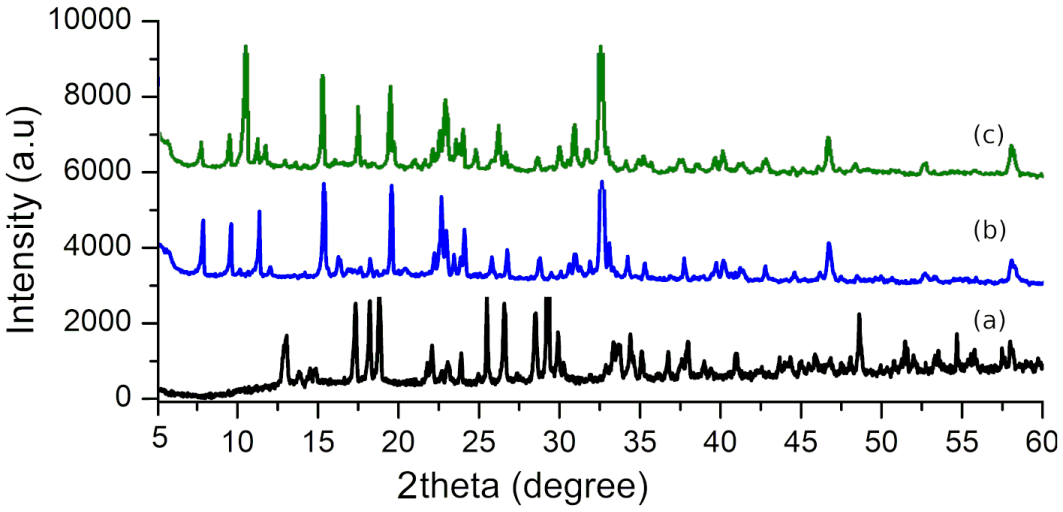

Figure IV.23 PXRD patterns of (a) **8**, (b) after exposing to NH_3 and (c) after heating.

The UV-visible absorption spectra of solid **8** exposed to NH_3 vapors also showed marked differences from the spectral pattern of the pure solid (Figure IV.24). Absorption bands of varying energies could be observed in addition to chloride-copper charge transfer bands which are due to changes in the ligand field around the metal, leading to significant changes in the d-d and/or LMCT absorption in solid **8** exposed to NH_3. The broad peak at around 650 nm can be attributed to d-d transition of Cu-ammonia complex, since peaks in the range 550-900 nm are general characteristics of $Cu(NH_3)_n^{2+}/Cu(NH_3)_n(H_2O)^{2+}_{6-n}$, n=0–4 species depending on the number of ammonia molecules involved in coordination [46]. Solid **8** exposed to NH_3 after heating (green form) also shows the absorption spectrum similar to the blue form, which indicated that there are no significant structural changes between the blue and the green forms.

The vapochromic response of **8** to NH_3vapours was further examined by TGA. Contrary to the TG curve of pure solid which shows weight loss at 100°C due to the loss of water molecule, solid **8** when exposed to ammonia showed initial weight loss at 50-70°C due to the loss of ammonia molecules (4%) incorporated in the crystal lattice. Subsequent

weight loss could be attributed to the release of organic moieties and chloride ions. TGA curve of **8** exposed to NH_3 after heating was similar and also shows small weight loss at around 70°C plausibly due to adsorbed moisture (Figure IV.25).

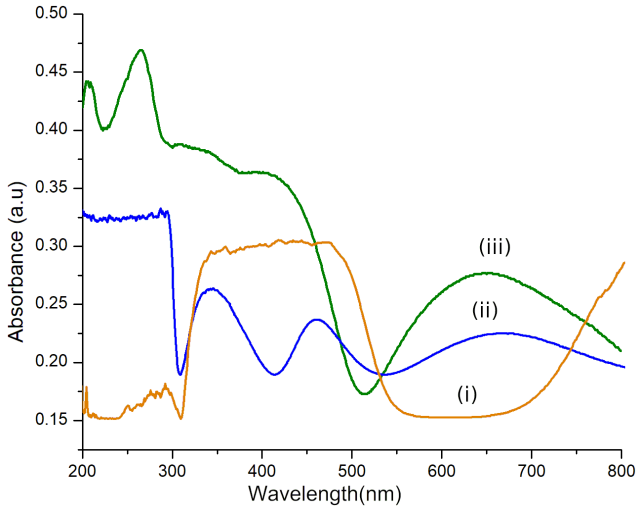

Figure IV.24 Solid state UV-Visible absorption spectra of (i) Solid **8**, (ii) **8** exposed to NH_3 and (iii) after heating.

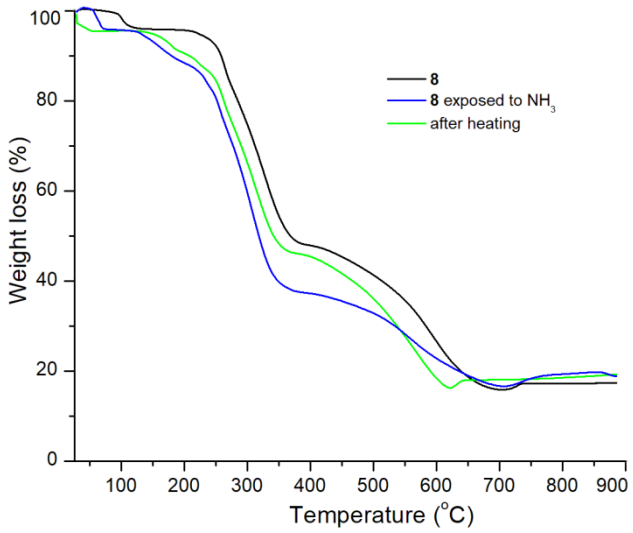

Figure IV.25 TGA curves of solid **8** exposed to NH_3vapors.

Based on the PXRD, TGA and UV-visible absorption spectra, the yellow-blue-green color variations exhibited by solid **8** when exposed to ammonia can be represented as shown in scheme IV.2.

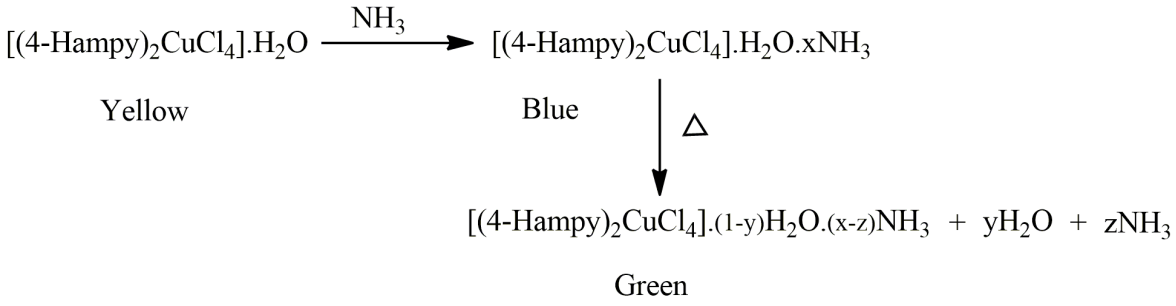

Scheme IV.2 Structural changes in solid **8** when exposed to NH_3.

IV.3.7.3 Investigation of thermochromism

Among the three solids, **8** also showed thermochromism wherein it displayed a change in color from yellow to orange upon heating to 100°C due to the loss of the water of crystallization. This observation was confirmed using TGA-DTA analysis. The dehydrated form could easily reverse to the original yellow state upon cooling to room temperature (Figure IV.26).

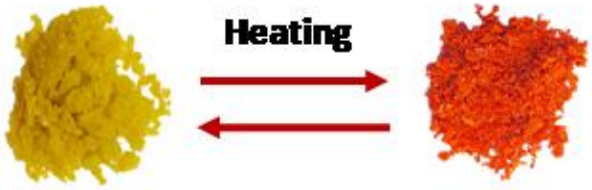

Figure IV.26 Thermochromism exhibited by **8**.

IV.4 Conclusions

In the present study, tetrachlorocuprates(II) of isomeric protonated aminopyridines were synthesized and characterized. Further the synthesized solids were examined for their ability to act as vapochromic sensors and they exhibited solvatochromism in the presence of selected solvents. **8** also exhibited reversible thermochromism. Chromotropism shown by these solids can be attributed to a synergy of various factors like changes in ligand field energy and supramolecular interactions such as hydrogen bonding. Tetrachlorocuprate(II) anions stabilized by protonated aminopyridines represent an interesting and significant class of chromogenic materials which may find applications in various fields like chemical sensors and detectors.

References

1. Golchoubian H, Mehrbanian D, Rezaee E, Xu ZX (2019) Transit Met Chem 44:671-680
2. Sone K, Fukuda Y (1987) Inorganic Thermochromism, Springer Berlin, Heidelberg
3. Liu JC, Liao WQ, Li PF, Tang YY, Chen XG, Song XJ, Zhang HY, Zhang Y, You YM, Xiong RG (2020) Angew Chem Int Ed 9:3495-3499
4. Bray KL, Drickamer HG (1990) J Phys Chem 94(5):2154-2159
5. Jaffe A, Lin Y, Mao WL, Karunadasa HI (2015) J Am Chem Soc 137(4):1673-1678
6. Dürr H, Bouas-Laurent H (2003) Photochromism: molecules and systems, Elsevier, Amsterdam
7. Riley MJ, Neill D, Bernhardt PV, Byriel KA, Kennard CHL (1998) Inorg Chem 37:3635-3639
8. Pan XW, Gang WV, Wang M, Chen HZ (2009) J Zhejiang Univ Sci A10:710-715
9. Li E, Jie K, Liu M, Sheng X, Zhua W, Huang F (2020) Chem Soc Rev 49:1517-1544
10. Hamaguchi T, Satomi N, Ando I (2018) Inorg Chim Acta 474:113-116
11. Golchoubian H, Ghorbanpour H, Rezaee E (2015) Inorg Chim Acta 442:30-36
12. Linert W, Fukuda Y, Camrad A (2001) Coord Chem Rev 218:113-152
13. Bares LA, Emerson K, Drumheller JE (1969) Inorg Chem 8:131-135
14. Steadman JP, Willett RD (1970) Inorg Chim Acta 4:367-371
15. Ferguson GL, Zaslow B (1971) Acta Crystallogr Sect B: Struct Sci Cryst Eng Mater 27:849-852
16. Anderson DN, Willett RD (1974) Inorg Chim Acta 8:167-175
17. Willet RD, Twamley B (2007) Acta Crystallogr E63:2591
18. Willett RD, Haugen JA, Lebsack J, Morrey J (1974) Inorg Chem 13(10):2510-2513
19. Harlow RL, Wells WJ, Watt GW, Simonsen SH (1974) Inorg Chem 13(9):2106-2111

20. Antolini L, Menabue L, Pellacani GC, Saladini M (1981) DaltonTrans 8:1753-1759
21. Bond MR, Johnson TJ, Willett RD (1988) Can J Chem 66:963-973
22. Battaglia LP, Corradi AB, Marcotrigiano G, Menabue L, Pellacani GC (1979) Inorg Chem18:148-152
23. Antolini L, Menabue L, Pellacani GC, Saladini M (1982) Inorg Chim Acta 58:193-200
24. Lahiry S, Sharma J, Sootha GD, Gupta HO (1978) Phys Stat Sol 46:153-162
25. Mostafa MF, Abdul-Kader MM, Arafat SS, Kandeel EM (1991) Phys Scr 43:627-629
26. Thomson RI, Rawson JM, Goeta A, Probert MR, Coome JA, Hoang TKA, Carpenter MA (2013) Mater Chem Phys 139:34-46
27. Fernández V, Doadrio JC, Granda SG, Pertierra P (1996) ActaCrystallogr Sect C: Cryst Struct Commun 52:1412-1415
28. Fernandez V, Torres MR, Tornero J (1997) Z Kristallogr NCS 212:377-378
29. Díaz I, Fernandez V, Belsky VK, Martinez JL (1999) Z Naturforsch B54:718-724
30. Haddad S, Willett RD (2001) Inorg Chem 40:2457-2460
31. Belsky VK, Fernandez V, Zavodnik VE, Diaz I, Martinez JL (2001) Crystallogr Rep 46(5):779-785
32. Bhattacharya R, Ray MS, Dey R, Righi L, Bocelli G, Ghosh A (2002) Polyhedron 21:2561-2565
33. Kelley A, Nalla S, Bond MR (2015) Acta Crystallogr Sect B: Struct Sci Cryst Eng Mater B71:48-60
34. Jaffe A, Karunadasa HI (2014) Inorg Chem 53(13):6494-6496
35. Mande HM, Ghalsasi PS, Navamoney A (2015) Polyhedron 91:141-149
36. Vishwakarma AK, Kumari R, Ghalsasi PS, Navamoney A (2017) J Mol Struct 1141:93-98

37. Kumar DK, Ballabh A, Jose DA, Dastidar P, Das A (2005) Cryst Growth Des 5(2):651-660
38. Halvorson KE, Patterson C, Willett RD (1990) Acta Cryst B46:508-519
39. Rietveld HM (1966) Acta Crystallogr 20:508-513
40. Spackman PR, Turner MJ, McKinnon JJ, Wolff SK, Grimwood DJ, Jayatilaka D, Spackman MA (2021) J Appl Cryst 54:1006-1011
41. Nakamoto K (1978) Infrared and Raman spectra of inorganic and coordination compounds, John Wiley & Sons, New York
42. Xiao F, Landee CP, Turnbull M, Wikaira JL (2019) Eur Chem Bull 8:239-243
43. Li L, Turnbull MM, Landee CP, Jornet J, Deumal M, Novoa J, Wikaira JL (2007) Inorg Chem 46:11254-11265
44. Willett RD, Liles OL Jr, Michelson C (1967) Inorg Chem 6(10):1885-1889
45. Elleb M, Meullemeestre J, Schwing-Weill MJ, Vierling F (1980) Inorg Chem 19:2699-2704
46. Trevani LN, Roberts JC, Tremaine PR (2001) J Solut Chem 30(7):585-622